Single-Crystal Silicon Thermal-Piezoresistive Resonators as High-Stability Frequency References

Connor A. Watkins, *Graduate Student Member, IEEE*, Jaesung Lee, *Member, IEEE*, Jonathan P. McCandless, *Member, IEEE*, Harris J. Hall, *Senior Member, IEEE*, and Philip X.-L. Feng, *Senior Member, IEEE*

***Abstract*— This paper reports on single-crystal silicon (Si) thermal-piezoresistive resonators (TPRs) achieving ∼0.2ppb-level frequency stability in phase-locked loop (PLL) measurements. A pair of resonators operating in a balanced-bridge configuration is presented, with one device being driven at resonance and the other used to null the parasitic background responses. The resonance frequency of the driven TPR has been measured over 40 hours with closed-loop continuous tracking by PLL and yields an Allan deviation $\sigma_A \approx 2.66$ppb at an averaging time of $\tau \approx 4.95$s which is the best reported value among all Si TPRs studied to date. Further, an external DC power feedback loop is implemented alongside the PLL to enhance the frequency stability of the TPR, to achieve $\sigma_A \approx 0.236$ppb at $\tau \approx 1.2$s, the best short-term frequency stability among all reported Si MEMS counterparts. This result suggests that such TPRs with precise DC control can potentially achieve frequency stabilities comparable to, or better than, existing state-of-the-art resonators used in oscillator circuits, with significantly reduced external thermal control requirements and power demands. [2024-0121]**

***Index Terms*— Microelectromechanical systems (MEMS) resonator, thermal-piezoresistive resonator (TPR), frequency stability, Allan deviation.**

Received 9 July 2024; revised 22 October 2024; accepted 11 November 2024. Date of publication 27 December 2024; date of current version 5 February 2025. This work was supported in part by the National Science Foundation (NSF) Industry-University Cooperative Research Centers (IUCRC) Program via the Multi-Functional Integrated System Technology (MIST) Center and its Research Internships for Graduate Students at Air Force Research Laboratory (NSF-AFRL INTERN) Program under Grant EEC-1939009 and in part by the NSF Division of Electrical, Communication & Cyber Systems (ECCS) EArly-concept Grants for Exploratory Research (EAGER) Program under Grant ECCS-2221881. The work of Connor A. Watkins was supported in part by the NSF Scholarship for Service (SFS) Fellowship at the University of Florida. Subject Editor H. Chang. *(Corresponding author: Philip X.-L. Feng.)*

Connor A. Watkins is with the Department of Electrical and Computer Engineering, University of Florida, Gainesville, FL 32611 USA (e-mail: watkins.connor@ufl.edu).

Jaesung Lee are with the Department of Electrical and Computer Engineering, University of Central Florida, Orlando, FL 32816 USA (e-mail: jaesung.lee@ucf.edu).

Jonathan P. McCandless was with the Air Force Research Laboratory, Wright-Patterson AFB, OH 45433 USA, and also with the Department of Electrical Engineering & Computer Science, Case Western Reserve University, Cleveland, OH 44106 USA. He is now with Gallox Semiconductors Inc., Ithaca, NY 14853 USA (e-mail: jmccandless@cornell.edu).

Harris J. Hall is with the Air Force Research Laboratory, Wright-Patterson AFB, OH 45433 USA (e-mail: harris.hall.3@us.af.mil).

Philip X.-L. Feng was with the Department of Electrical Engineering & Computer Science, Case Western Reserve University, Cleveland, OH 44106 USA. He is now with the Department of Electrical and Computer Engineering, University of Florida, Gainesville, FL 32611 USA (e-mail: philip.feng@ufl.edu).

Digital Object Identifier 10.1109/JMEMS.2024.3515098

I. Introduction

THERMAL-PIEZORESISTIVE resonators (TPRs) have recently been demonstrated as frequency-stable resonant microelectromechanical systems (MEMS). Among earlier TPRs, the piezoresistive MEMS heat engine was reported in 2011 [1]. There has been growing research to examine the effects of self-sustained oscillation (SSO) and thermal-piezoresistive feedback in these devices. To date, TPRs have been demonstrated for sensing [1], [2], [3], [4], [5] and signal amplification [6], [7], [8]. They are a new class of internally transduced resonant devices that can offer compelling performance benefits such as low motional resistance [9], high effective quality factor (Q_{eff}) [10], and reduced thermal control requirements, thanks to the thermal-piezoresistive internal feedback that is naturally built-in. Previous works have reported single-crystal Si TPRs with good frequency stabilities (*e.g.*, Allan deviation $\sigma_A \approx 40 \times 10^{-9}$ at $\tau \approx 0.02$s) while operating at their SSO thresholds [8], [11]. However, there has not been much research on the frequency stability of a single-crystal Si TPR operating below the SSO threshold.

In this work, we report on investigating the frequency stability of TPRs operating in a balanced-bridge circuit, with a phase-locked loop (PLL) employed to track the frequency of one of the resonators and an additional DC power feedback loop to further improve upon earlier reported stability results [12]. These resonators may have operating regimes of amplification and SSO similar to other reported TPRs [6], [7], [8] when driven at higher DC power levels than presented herein. However, here we do not pursue experimental identification of these regimes nor operation in them. Instead, operating well below any SSO threshold allows us to explore the optimal voltage coefficient of frequency (VCf) tuning needed to achieve superior frequency stability. All measurements are performed at room temperature under a moderate vacuum of ∼70mTorr. We achieve an Allan deviation (σ_A) of approximately 2.66ppb for an averaging time (τ) of 4.95s without DC power feedback, in comparison to $\sigma_A \approx 0.236$ppb at $\tau \approx 1.2$s with DC power feedback. Overall, our reported results are the best results reported for this class of devices with $\sigma_A \approx$ 40–90ppb for $\tau \approx$ 0.02–1s reported elsewhere in the literature [3], [4], [11] and among the best reported short-term frequency stability reported for any MEMS resonator [13], [14].

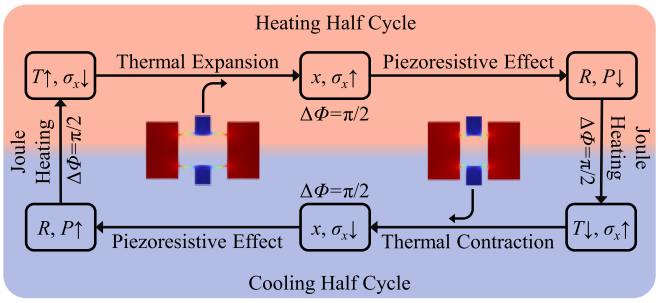

Fig. 1. Thermal-piezoresistive signal transduction block diagram describing how the TPR operates and illustrating the intrinsic internal feedback loop, depicting the changes in device temperature (T), actuator stress (σ_x), longitudinal actuator deformation (x), actuator resistance (R), and actuator power (P), with their respective physical effect causing the changes in device parameters. Insets show maximum expansion (contraction) of the longitudinal mode shape when heating (cooling) occurs in the TPR.

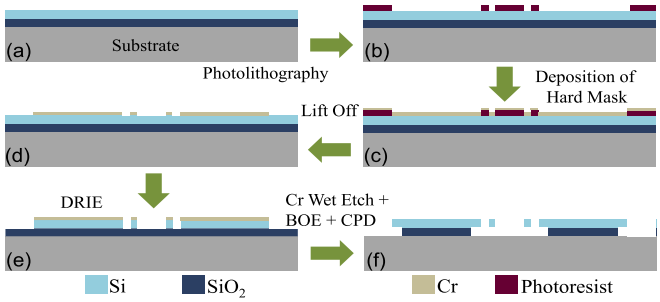

Fig. 2. Microfabrication of the Si TPR via an SOI wafer-based single-mask process for suspended resonators.

II. Device Fabrication and Operational Theory

The resonators are fabricated along the <100> direction of an n-type doped Si-on-insulator (SOI) wafer, with an estimated doping concentration of $N_d \approx 8 \times 10^{19}/\text{cm}^3$ calculated from Hall effect measurements, conditions that maximize the negative longitudinal piezoresistive coefficient $\pi_{11} = -102.2 \times 10^{-11}$ Pa^{-1} which is necessary for creating the thermal-piezoresistive feedback, as illustrated in Fig. 1. To fabricate the TPRs, a single-crystal SOI wafer-scale process for realizing suspended MEMS structures is used (Fig. 2). Fabrication starts with an SOI wafer (Fig. 2a) having 2μm-thick Si and 2μm-thick buried oxide (BOX, SiO_2) layers, with a photolithography step performed for hard mask patterning (Fig. 2b). A chromium (Cr) hard mask is then deposited (Fig. 2c), and lift-off is used to pattern it (Fig. 2d), which is followed by a dry etch of the Si device layer (Fig. 2e). Fabrication is finished by using a combination of Cr wet etching and buffered SiO_2 etchant to remove the hard mask and release the MEMS resonator, respectively. Finally, CO_2 critical point drying is performed to prevent stiction during the suspension of the resonators (Fig. 2f).

Each TPR is comprised of four Si piezoresistive beams, with a width of 1.74μm, length of 19μm, and thickness of 2μm, acting as electro-thermomechanical engines for the resonator when driven by both DC and AC (or radiofrequency, RF) currents, which are connected to a contact pad that also serves as a device anchor. Two identical proof masses are suspended to the piezoresistive beams (Fig. 3b). The specific design and fabrication of these TPRs leads to an entire suspended area that can be seen highlighted in Fig. 3c. In this work, we examine

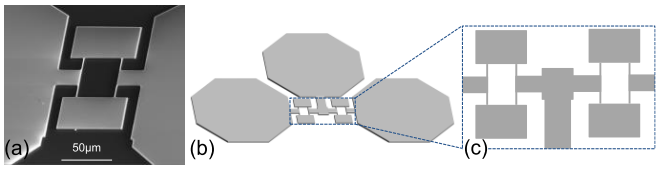

Fig. 3. Images of the TPRs and configuration of the TPRs studied in this work. (a) SEM image of a single TPR in this work, with a thickness of 2μm. (b) Structure and configuration of the TPRs, showing 2 TPRs connected via a suspended anchor from the middle pad, and with 3 large bonding pads. (c) Zoomed-in top view of the entire suspended region in the TPR-pair structure.

the potential of utilizing the TPR to generate a highly stable frequency reference. We hypothesize that the intrinsic internal feedback offers enhanced Q_{eff} which could contribute to a higher frequency stability.

III. Characterization of Resonators

A. Experimental Results of Individual Resonators

We first characterize the individual TPRs using a network analyzer and DC power source. The DC voltage is swept, which is used to Joule heat the beams, and the resonance characteristics are observed. Additionally, adjustments to the AC driving voltage are made to increase the signal-to-noise ratio (SNR) while avoiding a nonlinear response. We first configure TPR 1 into the experimental scheme seen in Fig. 4a and drive it until we observe an initial resonance (Fig. 4b). Afterwards, the TPR is driven by a larger AC signal plus a high DC bias to obtain a clear resonance that has good SNR (Fig. 4c). Finally, we perform a DC voltage sweep around 1V, to collect data for assessing the *voltage coefficient of frequency* ($\text{VC}f = (\Delta f/f_0)/\Delta V_{\text{dc}}$) as the biasing voltage is increased from 950mV to 1.05V (Fig. 4d).

An identical experimental scheme is again used to characterize TPR 2 (Fig. 4a) using the same network analyzer and DC power source. An initial resonance is observed for a DC voltage of 300mV (Fig. 4e) which has a lower SNR than TPR 1, resulting in a resonance peak that is more challenging to observe. To obtain a better SNR, and to ensure linear operation of the resonator, we drive TPR 2 with an AC voltage of 6mV (Fig. 4f). We then perform a DC sweep on TPR 2 to observe the frequency tuning by sweeping V_{dc} from 950mV to 1.05V and note that the resonant frequency continues to increase as the DC voltage is increased (Fig. 4g). Comparing the results of the DC sweeps of both TPRs 1 and 2 (Fig. 4d & Fig. 4g), we choose TPR 1 for further measurements, as it shows a $\text{VC}f = (\Delta f/f_0)/\Delta V_{\text{dc}} = 0$ at $V_{\text{dc}} = 980$mV. This will help minimize resonance frequency instability induced by fluctuations in the DC power source, potentially improving the expected frequency stability. We then extract the Q_{eff} of the TPR over the range of DC bias voltages employed and observe a slight improvement in Q_{eff} in our resonators as the DC voltage is increased (Fig. 4h).

B. Experimental Results of Balanced-Bridge Circuit

After we determine the individual device that will be used to perform further experiments, we connect both devices in a balanced-bridge circuit (Fig. 5a). The circuit enables us to

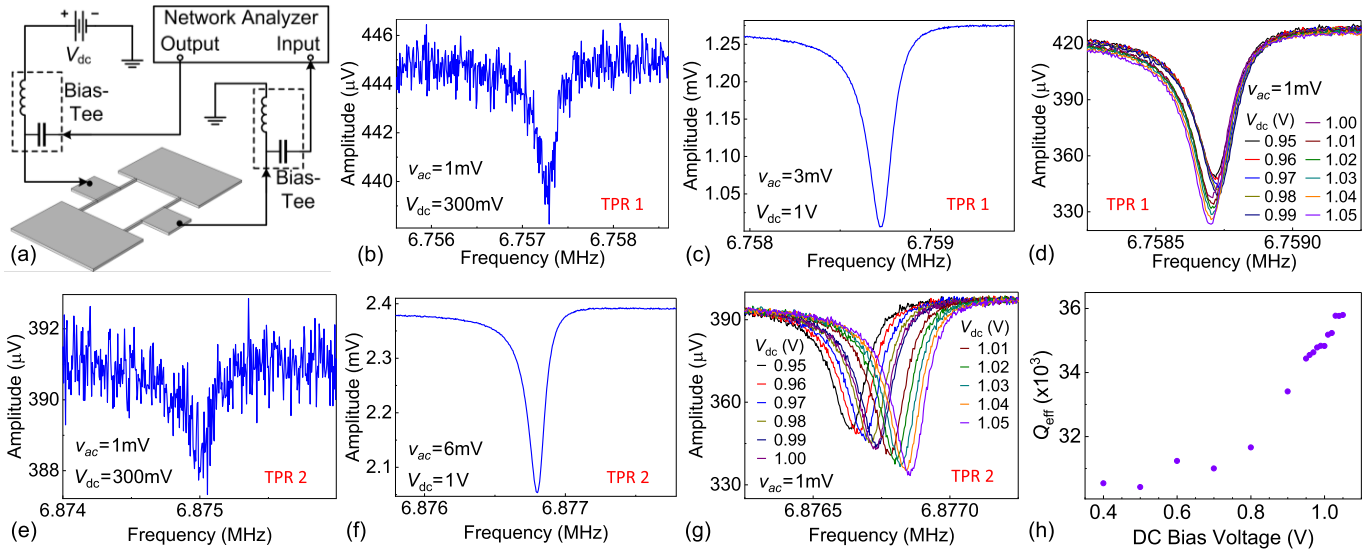

Fig. 4. Electrical measurement scheme of TPR 1 and TPR 2, and the subsequent measurement results. (a) Measurement circuit scheme for driving a single resonator and measuring its resonance response. (b) Initial resonance observed at a V_{dc} of 300mV and V_{ac} of 1mV for TPR 1. (c) Resonance of TPR 1 as V_{dc} is increased to 1V and V_{ac} is increased to 3mV, showing a clear resonance response with a Q_{eff} of 40,000. (d) Measurement of resonance response for TPR 1 when V_{ac} is set at 1mV and V_{dc} is swept from 950mV to 1.05V, showing small resonant frequency shifts as the DC bias voltage is increased. (e) Initial resonance observed at a V_{dc} of 300mV and V_{ac} of 1mV for TPR 2. (f) Resonance of TPR 2 as V_{dc} is increased to 1V and V_{ac} is increased to 6mV, showing a clear resonance response with a Q_{eff} of 42,000. (g) Measurement of resonance response for TPR 2 when V_{ac} is set at 1mV and V_{dc} is swept from 950mV to 1.05V, showing clearly noticeable resonant frequency shift as the DC bias voltage is increased. (h) Q_{eff} extraction over the range of DC bias voltages used to drive the resonators, with slight Q_{eff} improvement observed as V_{dc} is increased.

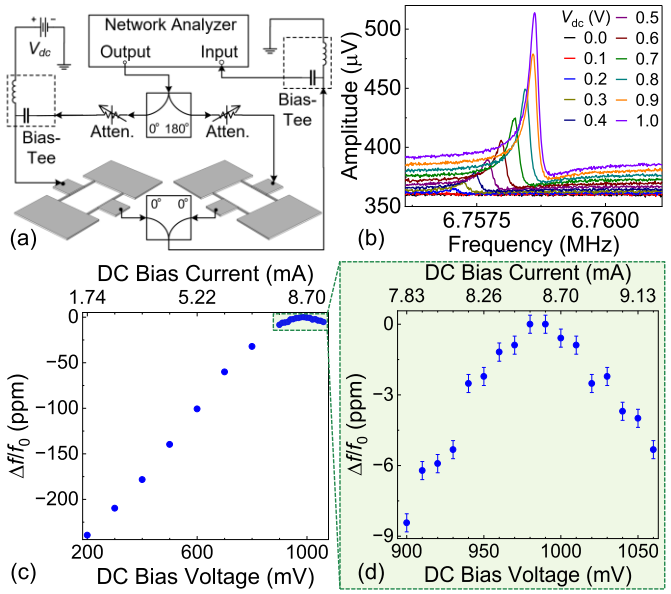

Fig. 5. Electrical measurement scheme for a pair of resonators operating in a balanced-bridge circuit, along with measurement results. (a) Measurement circuit scheme for driving TPR 1 at resonance while nullifying the background by driving a TPR 2 180° out of phase. (b) Frequency response of bridged circuit as V_{dc} is swept from 0mV to 1V. (c) Resonant frequency obtained from the TPR plotted against the DC bias voltage, as V_{dc} is swept from 200mV to 1.06V. A flattening of the frequency increase due to DC voltage increase is observed. (d) Zoomed-in view of (c) from 900mV to 1.06V plotted in ppm, showing the region where a zero-slope point for VCf = 0 is observed at V_{dc} = 980mV.

measure the resonant response of TPR 1 by driving it with both RF and DC currents, while driving TPR 2 solely with an RF current 180° out of phase, to provide real-time background subtraction. This circuit scheme allows us to perform subsequent measurements and characterization of individual resonators. We then characterize the resonator over a range of DC voltages (Fig. 5b). We find the highest resonance frequency of f = 6.759MHz at a corresponding DC bias voltage of V_{dc} = 980mV (Fig. 5c). This characterization is performed to ensure that we are operating the TPR at the zero-slope point of Fig. 5d to attain VCf = 0. Additionally, we employ the equivalent circuit model shown in Fig. 6a to extract circuit parameters by comparing the simulated curve obtained from the model to the experimental results (Fig. 6b). From the comparison, it is estimated that $Q_{eff} \approx$ 41,000 for the device connected in the balanced bridge circuit shown in Fig. 5a. The equivalent circuit model in Fig. 6a is comprised of several circuit elements which are shown in Fig. 6c. C_1 and C_2 describe the capacitance of the pads, where the chip is not grounded but is connected to the large ground plane present in the ceramic package. C_E is the electrical capacitance, arising from parasitic pad-to-pad capacitance, and R_A represents the electrical resistance, which is equivalent to the resistance from a single thermal beam due to the geometry of the resonator. R_m, L_m, and C_m are the motional impedance parameters of the MEMS resonator. All values for all circuit elements are shown in the table in Fig. 6c.

C. Modeling of Resonators to Determine VCf Rollover

When a TPR is electrically driven, the piezoresistive beams undergo Joule heating which both raises their temperature and induces stress from thermal expansion. Consequently, the negative temperature coefficient of Young's modulus (TCE_Y) in Si softens the longitudinal stiffness, reducing the resonance frequency. With the increase in thermal stress due to the elevated temperature, it is believed that the anchors of the TPR expand, causing an effective stiffness in the thermal beams to

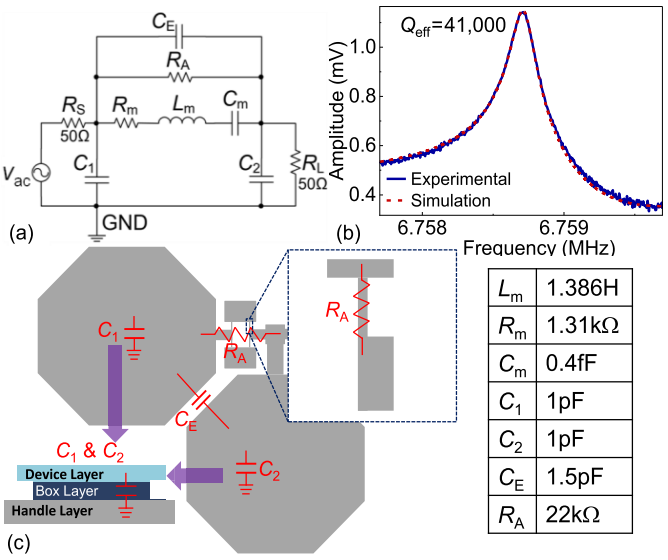

L_m	1.386H
R_m	1.31kΩ
C_m	0.4fF
C_1	1pF
C_2	1pF
C_E	1.5pF
R_A	22kΩ

Fig. 6. Equivalent circuit model and simulation results for a single resonator in a balanced-bridge configuration. (a) TPR equivalent circuit model showing where each component of the equivalent circuit model is obtained from, with the respective values for the circuit elements shown in the table on the bottom right. (b) Comparison of results from equivalent circuit simulation and experiment using the balanced-bridge (when V_{dc} = 980mV), showing a Q_{eff} of 41k that is obtained from the resonance fitting. (c) Equivalent circuit model for a single TPR without background, used for comparison to experimental results obtained from balanced-bridge configuration.

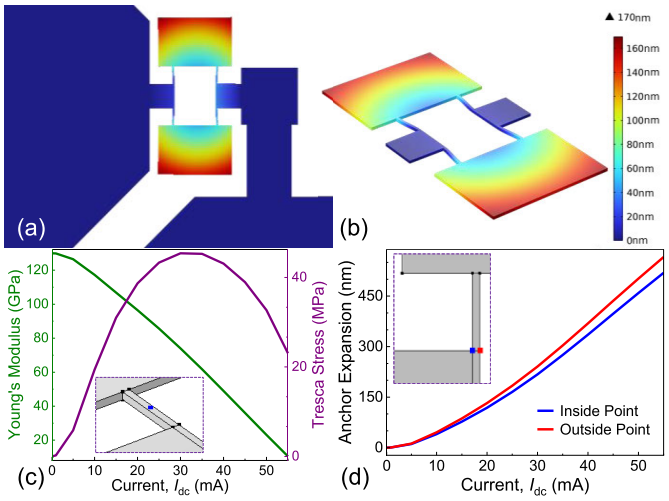

Fig. 7. Steady-state DC response from finite element method (FEM) simulations of a TPR using COMSOL MultiphysicsTM. (a) FEM model of a TPR, with thermal expansion color-plotted, when all geometry is modeled to accurately simulate the thermal expansion of the TPR when driven with a DC current. (b) Zoomed-in thermal expansion of a TPR when driven with I_{dc} = 7.5mA. (c) Young's modulus (EY) softening due to the increased temperature plotted against the Tresca stress in the beams at the middle point highlighted in the inset. (d) Expansion of the TPR anchor as I_{dc} is increased from 0mA to 55mA, with both points where the thermal beam connects to the anchor plotted, with an inset showing the two points highlighted in blue.

increase, subsequently raising the TPR's resonance frequency. In our measurement, we achieve VCf = 0 by balancing these two effects via carefully controlling V_{dc}, which can be observed in Fig. 5c.

COMSOL Multiphysics^{TM} finite element method (FEM) simulations have been performed on a TPR model for validation of the rollover point for VCf observed in Fig. 5d. We perform a steady-state DC response simulation on the TPR, to observe the electro-thermo-mechanical response of the TPR as a range of DC currents are simulated through the resonator. First, we start by simulating the electrothermal and thermomechanical responses of the resonator and surrounding geometry, including the BOX layer under the Si bonding pads (Fig. 7a), modeled with a temperature boundary condition of 293.15K at its bottom surface. We then observe the thermal expansion of the resonator as a range of DC currents are simulated through the model, with the octagonal electrical contact pads mechanically fixed. Fig. 7b shows a zoomed-in view of the resonator axial expansion as a 7.5mA DC current is simulated through it (Fig. 7b). We model the E_Y softening in the Si beams according to the equation in [15] and plot the E_Y softening compared to the Tresca stress in the middle of the thermal beams (Fig. 7c), to determine if our hypothesis for the resonance frequency increase as V_{dc} is increased is valid.

The Tresca stress (Fig. 7c) exhibits a rising trend until I_{dc} reaches 30 mA, beyond which it decreases, in line with our hypothesis regarding the rollover point seen in VCf in Fig. 5d. The finite element method (FEM) simulation results show an expansion (of width) in the anchors adjacent to the thermal beams, as depicted in Fig. 7d, thereby substantiating the hypothesis of increased effective stiffness in the thermal beams. In Fig. 5c, we note a turnover point for VCf at V_{dc} = 980 mV and I_{dc} = 8.5 mA, approximately 4 times lower than the values derived from our TPR model simulations. This discrepancy may stem from inaccuracies or oversimplifications in the heat transfer, surface-to-ambient radiation parameters, or other higher-order factors impacting the simulation outcomes. Future endeavors will need to focus on refining the electro-thermo-mechanical modeling of the TPRs to pinpoint the exact cause of the VCf rollover point. The models exhibit strong concurrence in validating the hypotheses concerning the VCf rollover points depicted in both Fig. 5c and Fig. 5d.

IV. Frequency Stability Measurements of Resonators

When tracking the frequency of a resonator, several random fluctuations in the resonance frequency will be present in the system and can be modeled using noise power laws [16]. The random fluctuations can be represented by the sum of five independent noise processes, which can be mapped onto an Allan deviation plot using the slope of $\sigma_A(\tau)$ to determine what power laws ($\tau^{\mu/2}$, with μ being the power index) the random fluctuations of the resonance frequency follow. Table I lists the five noise processes and the corresponding power laws for σ_A, each represented by a slope in the Allan deviation plot.

A. Frequency Stability of a TPR Operating in a PLL

After device characterization, we replace the network analyzer in Fig. 5a with a lock-in amplifier to construct a PLL to track the TPR 1 resonance frequency for ~40 hours to examine the stability of the resonance frequency. After 40 hours of testing, the resonance frequency has drifted about −3.6ppm and shows a linear variation over time (Fig. 8a). The observed frequency variation shows an apparent long-term frequency drift over the 40-hour measurement, which is hypothesized to be a result of a variation in the power delivered to the

TABLE I
MAPPING OF THE POWER LAW FREQUENCY MODULATION (FM) NOISE FOR FREQUENCY INSTABILITY OF OSCILLATORS USING ALLAN DEVIATION

Description of Noise Process	Power Law of $\sigma_A(\tau)$
Frequency Drift	τ^{1}
Random Walk FM	$\tau^{1/2}$
Flicker FM	τ^{0}
White FM	$\tau^{-1/2}$
White and Flicker Phase Modulation (PM)	τ^{-1}

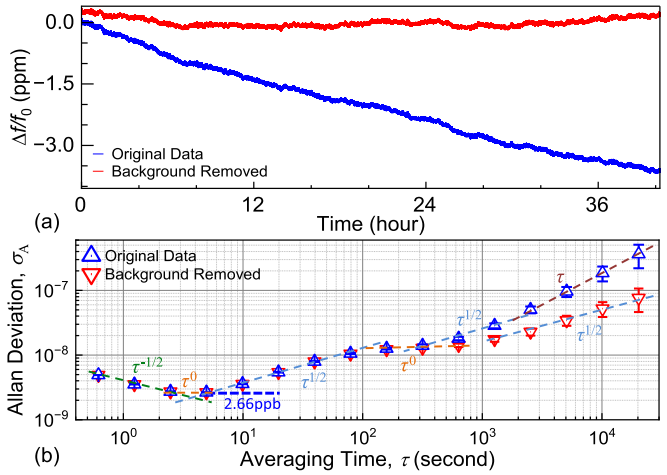

Fig. 8. Resonance frequency tracking results from a 40-hour PLL operation, along with respectively calculated σ_A results with $\tau^{\mu/2}$ power laws overlayed. (a) Measurement results from 40-hour PLL tracking resonance frequency of TPR 1 with (red) and without (blue) linear long-term frequency drift subtracted. (c) σ_A versus τ computed from the 40-hour PLL data, showing a minimum $\sigma_A = 2.66$ppb for original data (blue) and a lower σ_A at longer τ values with the linear background subtracted (red).

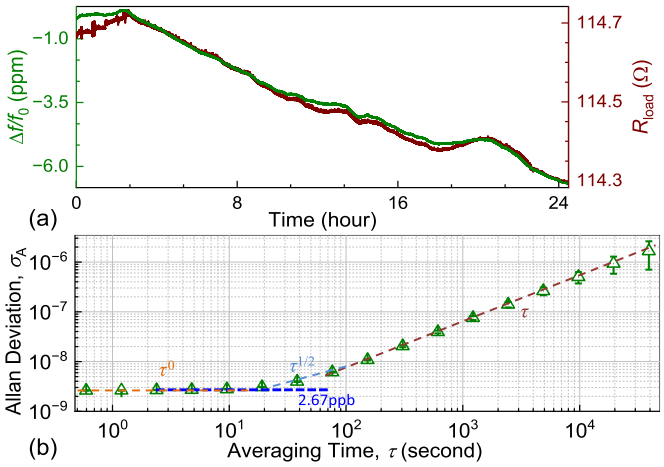

Fig. 9. Resonance frequency tracking results from a 24-hour PLL operation, along with calculated σ_A results with $\tau^{\mu/2}$ power laws overlayed, for verification of where linear long-term frequency drift arises from. (a) Measurement results from a 24-hour PLL with $I_{dc} = 7.5$mA delivered to a different resonator (TPR 3, green) while recording the total load resistance of the balanced-bridge circuit in Fig. 4a (maroon). (b) σ_A versus τ for 24-hour PLL data, showing a nearly flat minimum $\sigma_A = 2.67$ppb at a τ smaller than in results in Fig. 8, as well as long-term frequency stability that degrades at a faster rate than the previous measurement results of Fig. 8.

device. The power variation is thought to result from a change or drift in the electrical resistance of the device (R_A in Fig. 6a). If the linear long-term frequency drift is removed, the resultant frequency fluctuations are only a few hundred ppb, exhibiting excellent stability performance. The linear drift background-subtracted frequency variation data is a calculated result obtained by performing a linear fit to the frequency tracking data and then subtracting the resultant fit from the original data.

We then use the equation derived in Appendix I to calculate the Allan deviation from the 40-hour frequency stability measurement in Fig. 8a and obtain a σ_A of ≈2.66ppb for a τ of ≈4.95s (Fig. 8b). The background-subtracted PLL data shows better σ_A at larger τ values, following the random walk ($\tau^{1/2}$) power law for $\tau > 600$s, and identical σ_A at smaller τ values when compared to the original data.

To determine if the linear long-term frequency drift could be due to changes in electrical parameters, we run a 24-hour PLL with a constant current of $I_{dc} = 7.5$mA supplied by a Keithley 2450 SMU and track the change in load resistance (R_{load}). A different TPR (TPR 3, of geometry nearly equivalent to TPR 1) is used in this PLL, to determine whether or not the results are unique to the previous resonator (TPR 1). We note that the change in the resistance and frequency of the TPR circuit are in alignment and show a similar linear background response to that of the first pair of resonators that we measured (Fig. 8a). The clear overlap of the trends in $\Delta f/f_0$ and R_{load} traces confirm our hypothesis that the device resistance changes over the duration of the PLL, causing a linear long-term resonance frequency drift. We thus hypothesize that using an external feedback loop to supply constant DC power to the device could remove this linear background and produce results similar to that demonstrated in Fig. 8a with background subtraction.

From the 24-hour PLL measurement in Fig. 9a, the computed Allan deviation shows $\sigma_A \approx 2.67$ppb for $\tau \approx 2.39$s (marginally higher than results in Fig. 8), and noticeably compromised σ_A results for larger τ, following the τ^1 resonator frequency drift power law for $\tau > 50$s (Fig. 9b). Overall, we have achieved Allan deviation values that are approximately 15 to 35 times better than the reported values within the literature for similar devices operating at and below their SSO thresholds (Table II).

B. Constant DC Power Feedback for Stability Enhancement

We then create an external DC power feedback loop using a laptop computer equipped with LabVIEW (Fig. 10). A proportional, integral, and derivative (PID) controller is used to adjust the supplied V_{dc} by comparing the measured DC current to a target value set by the constant power criterion and calculating a new setpoint for V_{dc}. In the DC power feedback loop, we only use proportional (P) and integral (I) parameters because the derivative (D) parameter is sensitive to noise in the control system. The feedback loop has an adjustable measuring period, as well as an adjustable constant power setpoint and PID settings while the loop is running. We run this loop in parallel to a PLL for TPR 3 and track the resonance frequency and resistance (R_{load}) seen by the DC power supply over ∼23 hours (Fig. 11a). The PID controller is set with some initial parameters that appear to hold the DC power constant, though a drift in the R_{load} trace plotted Fig. 11a is observed. The drift in R_{load} appears to cause a corresponding drift in the resonance frequency. Calculating the Allan deviation of this

TABLE II
COMPARISON OF BEST REPORTED ALLAN DEVIATION FOR SEVERAL MEMS/NEMS RESONATORS

Reference	f_0	Resonator Dimensions	Heater Power	Material	Resonator Type	Q	Mode	Temperature Compensated	Best σ_A (τ)
[17]	220MHz	15μm × 200μm	-	AlN	CMR	1.40k	Contour	No, T≈20°C	9×10^{-8} (τ≈0.1s)
[18]	90kHz	90μm × 40μm	-	AlN	Cantilever	125	Flexural	No, T≈20°C	1×10^{-8} (τ≈10s)
[19]	1MHz	225μm × 110μm	0.9mW	Si	DETF	1.7k	Flexural	Yes, T≈110°C	32×10^{-9} (τ≈5s)
[20]	10.7MHz	300μm × 300μm	520.2mW	Si	Square Membrane	825k	Lamé	Yes, T≈-20°C	6×10^{-9} (τ≈100s)
[4]	929.2kHz	125μm × 145μm	-	Si	TPR	5.47k	Flexural	No, T≈20°C	89.07×10^{-9} (τ≈1s)
[21]	981.9kHz	280μm × 145μm	20mW	Si	DETF	18k	Flexural	Yes, T≈80°C	4.2×10^{-9} (τ≈100s)
	20.16MHz	400μm × 400μm	12mW	Si	Square Membrane	950k	Lamé	Yes, T≈60°C	6.5×10^{-10} (τ≈1000s)
[3]	5.13MHz	100μm × 160μm	-	Si	TPR	10.7k	Length Extensional	No, T≈20°C	85×10^{-9} (τ≈0.8s)
[11]	922.7kHz	830μm × 400μm	-	Si	TPR	1.06M	Length Extensional	No, T≈20°C	40×10^{-9} (τ≈0.02s)
[22]	65MHz	415μm × 43μm	-	AlN/Si	Bar Shaped	4.23k	Length Extensional	No, T≈20°C	4×10^{-9} (τ≈1s)
[12]	6.759MHz	80μm × 170μm	-	Si	TPR	41k	Length Extensional	No, T≈20°C	2.66×10^{-9} (τ≈4.95s)
This Work									2.36×10^{-10} (τ≈1.2s)

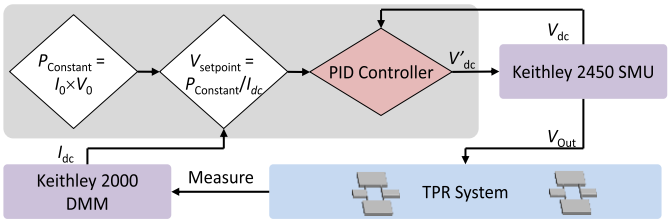

Fig. 10. Block diagram of external DC power feedback loop to enhance the stability of TPRs operating in PLL. By setting a constant power that the loop should aim to achieve, and by dividing the constant power by the DC current measured by a Keithley 2000 Digital Multimeter (DMM), a new DC voltage setpoint is obtained and fed to the PID controller to use in changing the voltage delivered by the Keithley 2450 SMU to the TPR system (of resonators).

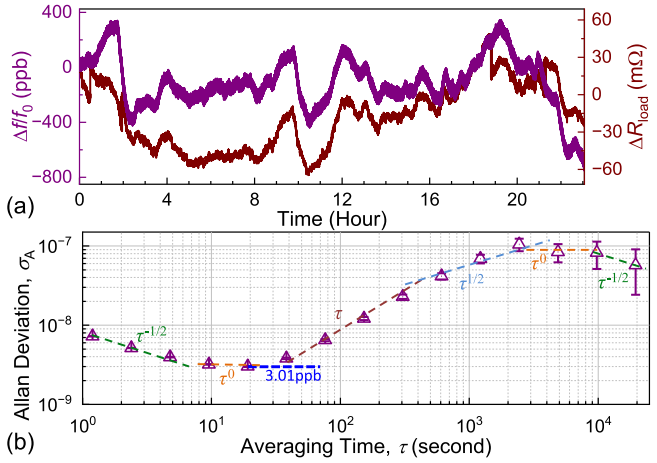

Fig. 11. Resonance frequency tracking results from a ~23-hour PLL operation using device TPR 3 and an external DC power feedback loop. (a) Measurement results from a 23-hour PLL (purple) with an external constant DC power feedback loop implemented while tracking the variations in R_{load}, plotted as ΔR_{load} = R_{load}−125.5Ω (maroon). (b) σ_A versus τ computed from the 23-hour PLL data with $\tau^{\mu/2}$ power laws overlayed, showing a minimum σ_A = 3.01ppb at τ = 19s, and long-term stability that stays just below 100ppb and starts to decrease at longer τ values.

frequency tracking we observe $\sigma_A \approx 3.01$ppb for $\tau \approx 19$s, comparable to our best results in Fig. 8 and Fig. 9, but with better long-term frequency stability (Fig. 11b). In the course of experimental handling, TPR 1 incurred accidental damage, rendering it unusable for further measurements. Therefore, all DC power feedback outcomes presented are based on TPR 3.

After our initial test of the PLL with an external DC power feedback loop implemented alongside it, we focus on tuning the PI parameters of the DC feedback loop for optimized stability in the DC power delivered to the resonator. We find that P = 0.2, I = 0.02, and D = 0 are ideal values for our PID controller and lead to the highest observed stability in our delivered DC power. After tuning the PID parameters of our DC power feedback, we again operate TPR 3 in a PLL alongside the DC power feedback loop, while tracking the resonance frequency and R_{load}. After running the PLL and DC power feedback loop for ~16 hours we observe a total resonance frequency shift of - 3.5ppm over the entire PLL operation time and a total R_{load} shift of only $\Delta R_{load} \approx \pm 20$mΩ (Fig. 12a). Calculating the Allan deviation of the resonance frequency results we obtain our best $\sigma_A \approx 0.236$ppb for a $\tau \approx 1.2$s, over an order of magnitude better than results shown in both Fig. 8 and Fig. 9, but with long-term stability that appears to be slowly degrading according to the power laws of resonator drift (τ^1) for $\tau \approx 10-1000$s and random walk ($\tau^{1/2}$) for averaging time beyond 1000s (Fig. 12b).

C. Comparison and Benchmarking of TPR Stability

The frequency stability results from implementing an external DC power feedback loop show promise for MEMS integration into frequency control and sensing applications. We compare the stability results from our TPRs versus the total motional area of the device's body (excluding pads or anchors or other non-motional parts), to frequency stability results from several state-of-the-art MEMS platforms (Fig. 13). Table II shows a comparison of our work to other reported MEMS/NEMS resonators with an emphasis on the best-reported Allan deviation while comparing multiple other parameters of the resonators. We observe enhanced short-term

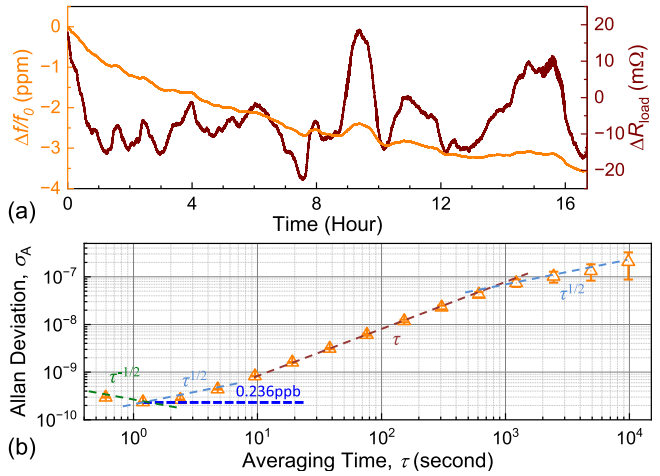

Fig. 12. Resonance frequency tracking results from a ∼16-hour PLL operation using TPR 3 and an external DC power feedback loop with better PID parameters tuning (only P & I in this case). (a) Measurement results from a 16-hour PLL (orange) with an external constant DC power feedback loop implemented while tracking the variations in R_{load}, plotted as $\Delta R_{load} = R_{load} - 124.86\Omega$ (maroon). (b) σ_A versus τ from the 16-hour PLL data with $\tau^{\mu/2}$ power laws overlayed, showing a minimum $\sigma_A = 0.236$ppb at $\tau = 1.2$s.

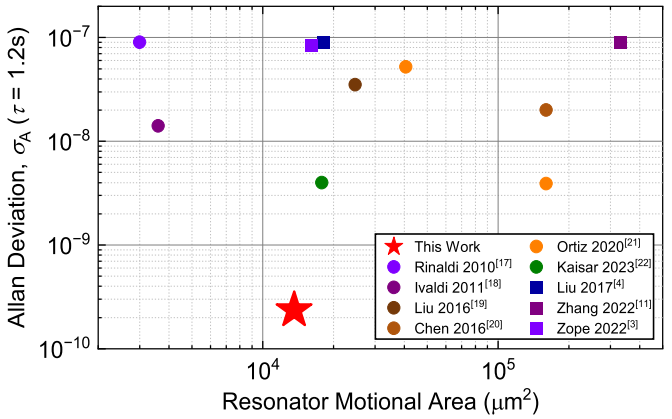

Fig. 13. Comparison plot of Allan deviation versus the total motional area of each device for various MEMS resonators including the TPR results shown in this work (star) and several state-of-the-art MEMS resonators (circles) and TPRs (squares) for timing and stability.

stability of 170−370 times better than other TPRs in the literature [3], [4], [11], [13], and 2.75−25 times better than even several MEMS resonators [17], [18], [19], [20], [21], [22] with external temperature control designed for long-term stability, with σ_A reported for $\tau = 100-1000$ seconds (Table II), enabled with a much smaller total resonator area (13.6×10^3 μm^2) than other devices.

We then compare the results from our earlier work in [12], where we have analytically subtracted a large linear background from a 40-hour PLL (Fig. 14a), to our PLL results with DC power feedback (Fig. 14b). After initial implementation of DC power feedback loop, stability is enhanced for longer τ but slightly degraded at shorter τ. This response is expected for our initial PID feedback control settings, as we have larger variations in R_{load} of the device compared to the plot in Fig. 12a and some instability present in the feedback loop. After fine tuning of the PID parameters, we not only observe enhanced stability at long averaging times, but also have improved the short-term stability by an order of magnitude (Fig. 14b).

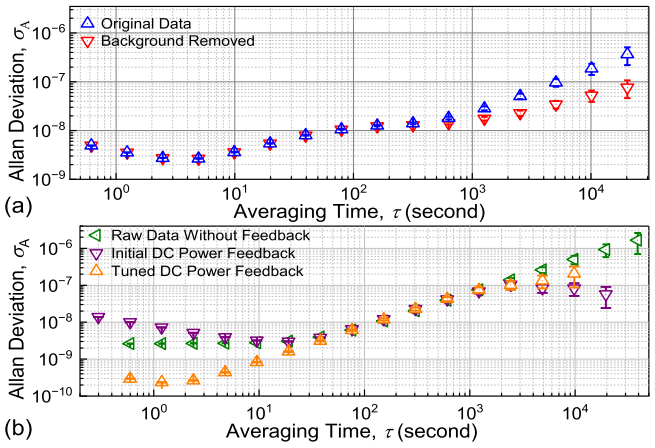

Fig. 14. Comparison plots of σ_A for PLL runs with and without DC power feedback loops for long-term linear background removal. (a) σ_A of TPR 1 with original PLL data (blue) and long-term linear background subtracted data (red). (b) σ_A of TPR 3 without external DC power feedback implemented alongside the PLL (green), an initial DC power feedback loop implemented alongside the PLL (purple), and a DC power feedback loop with optimally tuned PID parameters implemented alongside the PLL (orange).

D. Future Improvements to Device Stability

There are a few potential enhancements to our current measurement scheme that can be implemented to further improve the frequency stability of our TPRs. As we have shown above, using an external DC power supply feedback loop decreases the instability by removing the linear long-term background frequency drift. The resonance frequency and Q_{eff} of TPRs have been shown to exhibit temperature hysteresis with reduced temperatures [23] and a steep reduction in resonance frequency and flattening of Q_{eff} at higher currents and temperatures [24]. Thus, controlling the temperature fluctuations of the environment could also lead to an increased frequency stability and better σ_A for the TPRs. In addition, the PLL feedback loop implemented is limited to only frequency corrections due to phase differences in the AC input. Examining the inherent AC amplitude fluctuations and implementing additional AC power feedback may be appropriate to further improve frequency stability performance.

V. Conclusion

In conclusion, the results demonstrated herein represent a significant advancement in the measured frequency stability of Si TPRs, showcasing a substantial improvement exceeding an order of magnitude when compared to our previous work [12]. This has been made possible through the integration of an external constant DC power feedback loop in conjunction with a PLL for precise operation of TPR frequency tracking. The comprehensive experimentation has resulted in an exceptional Allan deviation of 0.236ppb for an averaging time of 1.2s during a 16-hour PLL measurement, all accomplished without the aid of external temperature control measures. The significance of our findings becomes even more apparent when juxtaposed against existing literature. Our results demonstrate a remarkable improvement, surpassing reported stability values for Si TPRs by 170 to 370 times. Further, our stability metrics also outperform those of MEMS resonators utilized in various

motion-readout modalities with external temperature control by a clear margin of 2.75 to 25 times. These outcomes validate the potential of Si TPR MEMS resonant sensors and timing devices, and underline their promises for applications requiring high precision and stability. Importantly, this study helps pave the way for further advancements in stability levels, particularly by refining environmental control mechanisms. Implementing strategies such as on-chip temperature regulation or enhancing vacuum levels holds promise for additional improvements in stability, thereby bolstering the credibility and applicability of Si TPR MEMS-enabled technologies for real-world scenarios.

Appendix
Determination of the Allan Deviation

To determine the frequency stability of a resonator or oscillator, the Allan deviation σ_{A} is computed [16], [25], [26], [27], [28], [29]. Allan deviation is defined as the deviation of variations between every two adjacent measured average fractional frequencies, as a function of the averaging time τ interval, with the instantaneous fractional frequency shift written as

$$y(t) = \frac{\delta f}{f_0} = \frac{f(t) - f_0}{f_0}, \tag{1}$$

where f_0 is the resonant frequency of the resonator and $f(t)$ is the measured frequency from the resonator at some time t. For computations of the Allan deviation in this work, the first resonance frequency point, $f(t=0)$, is used as f_0 and all other $f(t)$ are compared to that value. The measured value of the averaged fractional frequency shift for the ith time interval is defined as

$$\bar{y}_i = \frac{1}{m} \sum_{j=1+(i-1)m}^{im} y_i, \tag{2}$$

where m is defined as the averaging factor, an integer value related to τ as a multiple of the minimum time between discreet measurements τ_0. The rms fractional frequency shift is defined as

$$\langle y \rangle_\tau \equiv \left\langle \frac{\delta f}{f_0} \right\rangle_\tau \equiv \left\langle \frac{f - f_0}{f_0} \right\rangle_\tau, \tag{3}$$

where $\langle \ldots \rangle$ denotes an ideal ensemble average with infinite number of samples (each with time interval τ). For practical measurements, the rms fractional frequency shift is dependent on the final ensemble average as

$$\left\langle \frac{\delta f}{f_0} \right\rangle_\tau \cong \sqrt{\frac{1}{N-1} \sum_{i=1}^{N-1} \left(\frac{\bar{f}_{i+1} - \bar{f}_i}{f_0} \right)^2}, \tag{4}$$

where $\bar{f}_i$ is the measured average frequency in the ith discrete time interval of τ. The rms value is dependent on the sample standard deviation over the finite time interval.

The Allan variance is defined as the sample variance of two adjacent averages of the instantaneous fractional frequency fluctuation, which is expressed as

$$\sigma_{\mathrm{A}}^2(\tau) = \left\langle \left(\frac{\bar{y}_{i+1} - \bar{y}_i}{\sqrt{2}} \right)^2 \right\rangle. \tag{5}$$

Thus, the Allan variance from a finite data ensemble for a real measurement can be written as

$$\sigma_{\mathrm{A}}^2(\tau) = \frac{1}{2(N-1)} \sum_{i=1}^{N-1} \left(\frac{\bar{f}_{i+1} - \bar{f}_i}{f_0} \right)^2. \tag{6}$$

Since Allan deviation is defined as the square root of the Allan variance, it is written as

$$\sigma_{\mathrm{A}}(\tau) = \sqrt{\frac{1}{2(N-1)} \sum_{i=1}^{N-1} \left(\frac{\bar{f}_{i+1} - \bar{f}_i}{f_0} \right)^2}, \tag{7}$$

and is used to calculate the Allan deviation from the PLL frequency tracking results in this work.

References

[1] P. G. Steeneken et al., "Piezoresistive heat engine and refrigerator," *Nature Phys.*, vol. 7, no. 4, pp. 354–359, Apr. 2011.

[2] X. Guo, Y.-B. Yi, and S. Pourkamali, "Thermal-piezoresistive resonators and self-sustained oscillators for gas recognition and pressure sensing," *IEEE Sensors J.*, vol. 13, no. 8, pp. 2863–2872, Aug. 2013.

[3] A. Zope and S.-S. Li, "CMOS-MEMS thermal-piezoresistive resonators and oscillators for sensors," *Frontiers Mech. Eng.*, vol. 8, Jun. 2022, Art. no. 898668.

[4] T.-Y. Liu, C.-C. Chu, M.-H. Li, C.-Y. Liu, C.-Y. Lo, and S.-S. Li, "CMOS-MEMS thermal-piezoresistive oscillators with high transduction efficiency for mass sensing applications," in *Proc. 19th Int. Conf. Solid-State Sensors, Actuat. Microsystems (TRANSDUCERS)*, Jun. 2017, pp. 452–455.

[5] A. Quan et al., "A self-sustained mass sensor with physical closed loop based on thermal-piezoresistive coupled resonators," *IEEE Trans. Electron Devices*, vol. 69, no. 10, pp. 5808–5813, Oct. 2022.

[6] K. L. Phan et al., "High precision frequency synthesizer based on MEMS piezoresistive resonator," in *Proc. Transducers Eurosensors XXVII, 17th Int. Conf. Solid-State Sensors, Actuat. Microsyst. (TRANSDUCERS EUROSENSORS XXVII)*, Jun. 2013, pp. 802–805.

[7] A. Ramezany and S. Pourkamali, "Ultrahigh frequency nanomechanical piezoresistive amplifiers for direct channel-selective receiver front-ends," *Nano Lett.*, vol. 18, no. 4, pp. 2551–2556, Apr. 2018.

[8] H. Zhang, A. Quan, C. Wang, L. Wang, C. Wang, and M. Kraft, "A fast-startup self-sustained thermal-piezoresistive oscillaror with $>10^6$ effective quality factor in the air," in *Proc. IEEE 35th Int. Conf. Micro Electro Mech. Syst. Conf. (MEMS)*, Jan. 2022, pp. 142–145.

[9] A. Rahafrooz and S. Pourkamali, "Thermal-piezoresistive energy pumps in micromechanical resonant structures," *IEEE Trans. Electron Devices*, vol. 59, no. 12, pp. 3587–3593, Dec. 2012.

[10] J. M. L. Miller et al., "Thermal-piezoresistive tuning of the effective quality factor of a micromechanical resonator," *Phys. Rev. Appl.*, vol. 10, no. 4, Oct. 2018, Art. no. 044055.

[11] H. Zhang, A. Quan, C. Wang, C. Wang, L. Wang, and M. Kraft, "On the dynamic range and resolution of thermal-piezoresistive resonant mass sensors," *J. Microelectromech. Syst.*, vol. 31, no. 2, pp. 180–182, Apr. 2022.

[12] C. A. Watkins, J. Lee, J. P. McCandless, H. J. Hall, and P. X.-L. Feng, "Very high frequency stability of single-crystal silicon thermal-piezoresistive resonators with phase-locked loop," in *Proc. 22nd Int. Conf. Solid-State Sens., Act. Microsyst. (TRANSDUCERS)*, Jun. 2023, pp. 581–584.

[13] G. Sobreviela, X. Zou, C. Zhao, M. Pandit, and A. A. Seshia, "An ultra-high-quality factor silicon disk resonator," in *Proc. 20th Int. Conf. Solid-State Sensors, Actuat. Microsyst. Eurosensors XXXIII (TRANSDUCERS EUROSENSORS XXXIII)*, Jun. 2019, pp. 527–530.

[14] J. E.-Y. Lee, B. Bahreyni, Y. Zhu, and A. A. Seshia, "A single-crystal-silicon bulk-acoustic-mode microresonator oscillator," *IEEE Electron Device Lett.*, vol. 29, no. 7, pp. 701–703, Jul. 2008.

[15] C.-H. Cho, "Characterization of young's modulus of silicon versus temperature using a 'beam deflectio' method with a four-point bending fixture," *Current Appl. Phys.*, vol. 9, no. 2, pp. 538–545, Mar. 2009.

[16] W. Riley and D. Howe, "Handbook of frequency stability analysis," Nat. Inst. Stand. Tech., Gaithersburg, MD, USA, Tech. Rep. NIST SP 1065, 2008.

[17] M. Rinaldi, B. Duick, C. Zuniga, C. Zuo, and G. Piazza, "SS-DNA functionalized ultra-thin-film ALN contour-mode resonators with self-sustained oscillator for volatile organic chemical detection," in *Proc. IEEE 23rd Int. Conf. Micro Electro Mech. Syst. (MEMS)*, Jan. 2010, pp. 132–135.
[18] P. Ivaldi et al., "50 nm thick AlN film-based piezoelectric cantilevers for gravimetric detection," *J. Micromech. Microeng.*, vol. 21, no. 8, Jul. 2011, Art. no. 085023.
[19] C.-Y. Liu, M.-H. Li, H. G. Ranjith, and S.-S. Li, "A 1 MHz 4 ppm CMOS-MEMS oscillator with built-in self-test and sub-mW ovenization power," in *IEDM Tech. Dig.*, Dec. 2016, pp. 651–654.
[20] Y. Chen et al., "Ovenized dual-mode clock (ODMC) based on highly doped single crystal silicon resonators," in *Proc. IEEE 29th Int. Conf. Micro Electro Mech. Syst. (MEMS)*, Jan. 2016, pp. 91–94.
[21] L. C. Ortiz et al., "Low-power dual mode MEMS resonators with PPB stability over temperature," *J. Microelectromech. Syst.*, vol. 29, no. 2, pp. 190–201, Apr. 2020.
[22] T. Kaisar et al., "Five low-noise stable oscillators referenced to the same multimode AlN/Si MEMS resonator," *IEEE Trans. Ultrason., Ferroelectr., Freq. Control*, vol. 70, no. 10, pp. 1213–1228, Oct. 2023.
[23] J. M. L. Miller et al., "Limits to thermal-piezoresistive cooling in silicon micromechanical resonators," *J. Microelectromech. Syst.*, vol. 29, no. 5, pp. 677–684, Oct. 2020.
[24] J. M. L. Miller et al., "Temperature hysteresis in piezoresistive microcantilevers," in *Proc. IEEE 33rd Int. Conf. Micro Electro Mech. Syst. (MEMS)*, Jan. 2020, pp. 1203–1206.
[25] *IEEE Standard Definitions of Physical Quantities for Fundamental Frequency and Time Metrology—Random Instabilities*, IEEE Standard 1139-2008, Feb. 2009.
[26] J. A. Barnes et al., "Characterization of frequency stability," *IEEE Trans. Instrum. Meas.*, vol. IM-20, no. 2, pp. 105–120, May 1971.
[27] M. Sansa et al., "Frequency fluctuations in silicon nanoresonators," *Nature Nanotechnol.*, vol. 11, no. 6, pp. 552–558, Jun. 2016.
[28] J. Rutman and F. L. Walls, "Characterization of frequency stability in precision frequency sources," *Proc. IEEE*, vol. 79, no. 7, pp. 952–960, Jul. 1991.
[29] D. W. Allan, "Time and frequency (time-domain) characterization, estimation, and prediction of precision clocks and oscillators," *IEEE Trans. Ultrason., Ferroelectr. Freq. Control*, vol. UFFC-34, no. 6, pp. 647–654, Nov. 1987.

Connor A. Watkins (Graduate Student Member, IEEE) received the B.S. degree in electrical engineering from the University of West Florida (UWF), Pensacola, FL, USA, in 2018. He is currently pursuing the Ph.D. degree in electrical and computer engineering with the University of Florida (UF), Gainesville, FL. His major research interests include frequency stability analysis in micro/nanoelectromechanical systems (MEMS/NEMS) resonators for frequency reference and clock applications, noise analyses in MEMS/NEMS resonators, metamaterials, and micro/nanofabrication. He was a recipient of the University of Florida NSF SFS Fellowship from 2020 to 2023 and the NSF AFRL-INTERN Internship Award Program from 2023 to 2024.

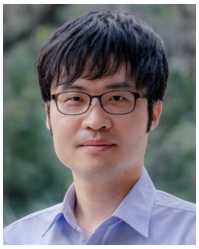

Jaesung Lee (Member, IEEE) received the B.S. and M.S. degrees in electrical engineering from The University of Electro-Communications (UEC), Tokyo, Japan, in 2007 and 2009, respectively, and the Ph.D. degree in electrical engineering from Case Western Reserve University (CWRU), Cleveland, OH, USA, in 2017. He is currently an Assistant Professor with the Department of Electrical and Computer Engineering, University of Central Florida, Orlando, FL, USA. His research has focused on developing functional nanodevices (e.g., NEMS/MEMS, optoelectronic, and phononic devices) using advanced materials (e.g., 2-D crystals and wide bandgap semiconductors), toward building integrated systems for signal processing and sensing, in both classical and quantum regimes. He is the Technical Program Chair of the MEMS/NEMS Technical Group, 70th American Vacuum Society (AVS) International Symposium and Exhibition.

Jonathan P. McCandless (Member, IEEE) received the B.S.E. degree in electrical engineering from Case Western Reserve University, Cleveland, OH, USA, in 2016, the B.S. degree in engineering physics from John Carroll University, University Heights, OH, and the Ph.D. degree in electrical and computer engineering from Cornell University, Ithaca, NY, USA. He studied MBE growth and transport of Ga_2O_3 and related alloys from Cornell University. Currently, he is an Ignite Post-Doctoral Fellow with Cornell University, working on commercialization of Ga_2O_3 for power electronics. Prior to Cornell, he was with the Air Force Research Laboratory (AFRL), Dayton, OH, USA, focusing on device fabrication and testing of GaN and Ga_2O_3 devices. He was a recipient of the 2019 NSF Graduate Research Fellowship (GRFP) and an Irwin Jacobs Family Fellow. In 2021, he received a German Academic Exchange Service (DAAD) Fellowship to study polarization induced electron transport in nitride heterostructure with the University of Bremen. He received Best Student Presentation Awards in 2021 and 2022 from Electronic Materials Conference (EMC) and the International Workshop on Gallium Oxide (IWGO), respectively.

Harris J. Hall (Senior Member, IEEE) received the B.S. degree in electrical engineering from Rensselaer Polytechnic Institute in 1999, the M.S. degree in electrical engineering from the Air Force Institute of Technology in 2001, and the Ph.D. degree in mechanical engineering (microsystems) from the University of Colorado Boulder in 2013. He is a Senior Research Electronics Engineer with the Air Force Research Laboratory's (AFRL) Sensors Directorate. He became a member of AFRL's Technical Staff later that year. His current research interests include microelectromechanical systems (MEMS), resonators, nanoscale vacuum emission electronics, photoactive microstructures, and heterogeneous integration of RF passive components.

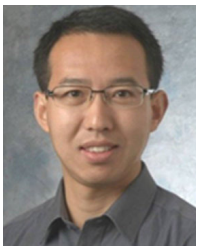

Philip X.-L. Feng (Senior Member, IEEE) received the Ph.D. degree in electrical engineering (EE) from California Institute of Technology (Caltech), Pasadena, CA, USA, in 2007. He is currently a Wally Rhines Endowed Professor with the Department of Electrical and Computer Engineering, University of Florida, Gainesville, FL, USA. He has mentored 15 Ph.D. students to successful dissertation defense, mentored ten post-doctoral scholars, and also supervised 16 M.S. students with theses or research projects. His research is primarily focused on emerging solid-state devices and systems, particularly nano/microelectromechanical systems (NEMS/MEMS), atomic layer semiconductors and 2D heterostructure devices, silicon carbide (SiC) and other wide/ultrawide-bandgap (WBG/UWBG) semiconductors, quantum devices based on SiC and 2D materials, and their integration with state-of-the-art ICs and optical/photonic technologies. He was an invited participant to the National Academy of Engineering (NAE) U.S. Frontiers of Engineering (USFOE) Symposium in 2013. Subsequently, he was a recipient of the NAE Grainger Foundation Frontiers of Engineering (FOE) Award in 2014. His other awards include the National Science Foundation (NSF) CAREER Award in 2015 and the Presidential Early Career Award for Scientists and Engineers (PECASE) in 2019. He and his students have won seven best paper/presentation awards from IEEE and other international conferences. He has served on the Technical Program Committees (TPCs) for the IEEE International Electron Devices Meeting (IEDM); IEEE International Conference on Micro Electro Mechanical Systems (MEMS); International Conference on Solid-State Sensors, Actuators and Microsystems (Transducers); International Frequency Control Symposium (IFCS); IEEE SENSORS, and other international conferences. He served as a Track Chair for IEEE SENSORS from 2016 to 2017 and the TPC Group IV Chair for IEEE IFCS from 2018 to 2020. He has also served as the Technical Program Chair for the MEMS/NEMS Technical Group from the 61st to 63rd American Vacuum Society (AVS) International Symposium and Exhibition. Since 2017, he has been a Co-Organizer and the Technical Chair of the SiC + X Materials and Devices Workshop. He has served as a Chair for the 34th IEEE International Conference on Micro Electro Mechanical Systems (IEEE MEMS 2021). He has also Co-Organized and Co-Chaired the Florida Semiconductor Week (FSW) Workshop in January 2023.